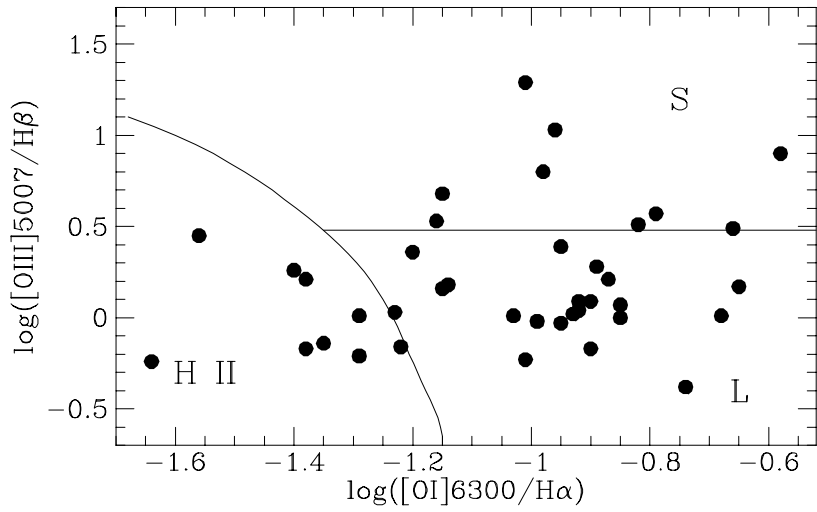
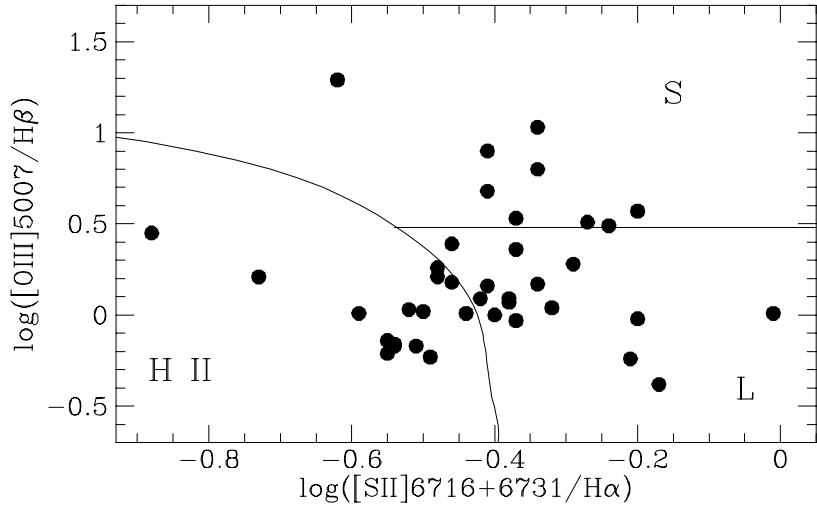
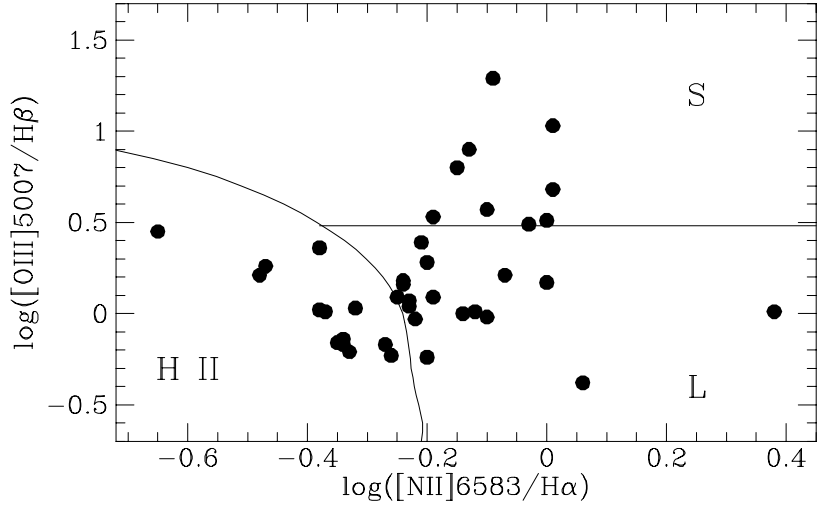


This figure "fig1_1.jpg" is available in "jpg" format from:

<http://arxiv.org/ps/astro-ph/9806149v1>

This figure "fig1_2.jpg" is available in "jpg" format from:

<http://arxiv.org/ps/astro-ph/9806149v1>



THE *IRAS* 1-JY SAMPLE OF ULTRALUMINOUS INFRARED GALAXIES: II. OPTICAL SPECTROSCOPY¹

D.-C. Kim,^{2,3} Sylvain Veilleux,⁴ and D. B. Sanders⁵

ABSTRACT

This is the second paper in a series discussing the properties of ultraluminous infrared galaxies (ULIGs: $L_{\text{ir}} > 10^{12} L_{\odot}$; $H_o = 75 \text{ km s}^{-1} \text{ Mpc}^{-1}$ and $q_o = 0.0$) from the 1-Jy sample of Kim (1995). This paper presents the first results of a spectroscopic survey at optical wavelengths of a randomly selected subset of 45 ULIGs from Kim & Sanders (1997). These new data are combined with previous data from Veilleux et al. (1995) to determine the spectral properties of luminous infrared galaxies (LIGs) with $L_{\text{ir}} \approx 10^{10.5} - 10^{13} L_{\odot}$. We find that the fraction of Seyfert galaxies among LIGs increases dramatically above $L_{\text{ir}} \approx 10^{12.3} L_{\odot}$ — nearly half of the galaxies with $L_{\text{ir}} > 10^{12.3} L_{\odot}$ present Seyfert characteristics. Many of the optical properties of these Seyfert galaxies are consistent with the presence of a genuine active galactic nucleus (AGN) in the core of these objects.

The continuum colors and strengths of the stellar $H\beta$ and Mg Ib features in and out of the nuclei of ULIGs indicate that star formation has recently ($\sim 10^7$ yr) taken place in the nuclear and circumnuclear regions of many of these objects. As expected, photoionization by hot stars appears to be the dominant source of ionization in the objects with H II region-like spectra. Evidence is presented that the ionization source in infrared-selected galaxies with nuclear LINER-like spectra (38% of the ULIGs in our sample) is likely to be shocks or of stellar origins rather than an AGN. Shock ionization associated with starburst-driven outflows may also explain the LINER-like emission detected *outside* the nuclei of some galaxies.

No significant differences are found between the mean color excess of ULIGs and that of *IRAS* galaxies of lower infrared luminosity. However, in contrast to what was found in low-luminosity infrared galaxies, the color excess in the nuclei of ULIGs does not seem to depend on spectral types. The reddening in ULIGs is generally observed

¹This work was part of a Ph.D. thesis by D.-C. Kim completed in the Department of Physics and Astronomy, University of Hawaii, Honolulu, HI

²Current address: Infrared Processing and Analysis Center, California Institute of Technology, Pasadena, CA 91125; E-mail: kim@ipac.caltech.edu

³Institute for Astronomy, University of Hawaii, 2680 Woodlawn Drive, Honolulu, HI 96822

⁴Department of Astronomy, University of Maryland, College Park, MD 20742; E-mail: veilleux@astro.umd.edu

⁵Institute for Astronomy, University of Hawaii, 2680 Woodlawn Drive, Honolulu, HI 96822; sanders@ifa.hawaii.edu

to decrease with distance from the nucleus as in their low-luminosity counterparts. Clear cases of inverted reddening profiles are observed in less than 1/5 of the ULIGs in our sample, nearly all of which are optically classified LINERs. These profiles may reflect the actual dust distribution in these objects or may be due to complex optical depth effects.

Subject headings: galaxies: nuclei — galaxies: stellar content galaxies : Seyfert — infrared: sources

1. Introduction

Over the last decade, several spectroscopic studies have attempted to determine the nature of the dominant energy source in ultraluminous infrared galaxies (ULIGs: $L_{\text{ir}} > 10^{12} L_{\odot}$)⁶. Spectroscopic surveys of unbiased samples of luminous *IRAS* galaxies (e.g. Elston, Cornell, & Lebofsky 1985; Leech et al. 1989; Allen et al. 1991; Ashby, Houck, & Matthews 1995) generally have found that $\gtrsim 80\%$ of high-luminosity infrared galaxies ($L_{\text{ir}} > 10^{11} L_{\odot}$) present H II region-like optical spectra, and therefore appear to be powered by hot stars rather than an active galactic nucleus (AGN). However, the great majority of the infrared galaxies in these samples are in the luminosity range $L_{\text{ir}} = 10^{11} - 10^{12} L_{\odot}$, with only a few having $L_{\text{ir}} > 10^{12} L_{\odot}$. This distinction is important as there is growing evidence that the fraction of AGN among LIGs increases with increasing L_{ir} (see review by Sanders & Mirabel 1996). An early analysis by Sanders et al. (1988) of 10 ULIGs in the Bright Galaxy Survey (BGS: Soifer et al. 1987, 1989) suggested that 9 of these objects had AGN-like optical spectra (i.e. either Seyferts or LINERs). In addition, Armus, Heckman & Miley (1989) found that 10 of the 12 ULIGs in their sample of slightly more distant objects presented AGN-like spectra. More recently, Veilleux et al. (1995; hereafter VKSMS) carried out a sensitive spectroscopic survey of a sample of 200 LIGs and classified the nuclear spectra of these galaxies using a large number of line-ratio diagnostics corrected for the underlying stellar absorption features. They found that 13 of the 21 ULIGs in their sample (including the 10 ULIGs from the BGS) showed AGN-like spectra.

Although the results from previous spectroscopic surveys of ULIGs are important, the relatively small number of objects studied, the limited range of L_{ir} of these objects (nearly all have $L_{\text{ir}} < 10^{12.3} L_{\odot}$), and the relatively low resolution and modest signal-to-noise of many of the spectra, make it desirable to obtain more sensitive and higher resolution data for a larger sample of objects. The recent publication of the 1-Jy sample of ULIGs (Kim & Sanders 1997; hereafter Paper I) provides such a sample that can now be used for a more complete study of the properties

⁶ $L_{\text{ir}} \equiv L(8 - 1000\mu\text{m})$, computed from the observed infrared fluxes in all four *IRAS* bands according to the prescription outlined in Perault (1987). We assume $H_0 = 75 \text{ km s}^{-1} \text{ Mpc}^{-1}$ and $q_0 = 0$ throughout this paper.

of ULIGs. The 1-Jy survey contains a complete sample of 111 ULIGs ($|b| > 30^\circ$, $\delta > -40^\circ$) plus a smaller supplementary list of 8 ULIGs at lower Galactic latitude ($|b| = 20^\circ - 30^\circ$) that were selected from the *IRAS* Faint Source Catalog–Version 2 (FSC: Moshir et al. 1992) on the basis of their $60\mu\text{m}$ flux: $f_{60} > 1\text{-Jy}$ ⁷ (see Paper I for a complete description of the sample and selection criteria).

This paper presents the first results from a spectral analysis of a randomly selected subset of 45 ULIGs selected from Paper I. Spectra on the remaining objects in the 1-Jy sample have been collected and are presently being analyzed (Veilleux, Kim, & Sanders 1997a). The current subsample, which includes 35% of the total number of objects in the complete 1-Jy survey, was selected to be fairly evenly distributed in redshift, and should be representative of the complete 1-Jy sample. Unlike previous spectroscopic studies of ULIGs, where the majority of objects have $L_{\text{ir}} < 10^{12.3} L_\odot$, the current survey has a large fraction of objects ($\sim 45\%$) with higher luminosity ($L_{\text{ir}} = 10^{12.3} - 10^{12.9} L_\odot$), and thus provides for the first time a more realistic picture of the spectroscopic properties of ULIGs throughout the decade luminosity range $L_{\text{ir}} = 10^{12} - 10^{13} L_\odot$. Section 2 discusses the procedures used to obtain and reduce the new data. Details of the line and continuum measurements are discussed in §3. The spectral analysis was carried out in both the nuclear and circumnuclear regions of these galaxies. The results derived from the nuclear spectra are described in §4, while the radial profiles of a number of spectral parameters are analyzed in §5. The main conclusions are summarized in §6.

2. Observations and Data Reduction

All of the spectroscopic data were obtained with the Faint Object Spectrograph at the f/10 Cassegrain focus of the University of Hawaii 2.2-m telescope on Mauna Kea. Table 1 lists the dates of the observations, grating used, spectral coverage, resolution, seeing, and detectors used for the observations. The exposure times range from 300 sec to 2,000 sec depending on the R magnitude of each object (see Kim, Sanders & Mazzarella 1996; hereafter Paper III). In all cases, a slit with a width of $2''$ was used and the slit was positioned in the E-W direction ($PA = 90^\circ$). All observations were made under photometric conditions.

The reduction techniques of Kim et al. (1995) were used to reduce the present data. To minimize aperture-related effects, the window used for the extraction of the nuclear spectrum was varied according to the redshift of each object so that it corresponds to a constant linear scale (total diameter) of 4 kpc for most of the galaxies, with the exceptions of five distant galaxies with $z > 0.15$ (FSC 10091+4704, FSC 11582+3020, FSC 13218+0552, FSC 14070+0525, and FSC 16300+1558)⁸ for which an 8-kpc window was used. Note, however, that the effective size

⁷The quantities f_{12} , f_{25} , f_{60} , f_{100} , are the *IRAS* flux densities in Jy at $12\mu\text{m}$, $25\mu\text{m}$, $60\mu\text{m}$, and $100\mu\text{m}$ respectively

⁸Object names that begin with ‘FSC’ are sources identified in the *IRAS* Faint Source Catalog–Version 2 (Moshir

of the aperture still has a dependence on redshift since the slit width was held constant at $2''$ during all of the observations. The resulting spectra contained absorption bands near 6870 \AA and 7620 \AA produced by atmospheric O_2 (the B- and A-bands, respectively). These features were removed using the spectra of the flux standard stars.

3. Line and Continuum Measurements

The final calibrated spectra are plotted in Figure 1. Table 2 lists the measured redshifts, the infrared luminosities computed from these redshifts using the procedure outlined in Kim et al. (1995), and the spectral type as determined from the spectra in Figure 1 (see §4.1). Also listed for completeness in Table 2 are the basic properties of 7 other ULIGs from the 1-Jy sample for which spectroscopic data already exist in the literature. However, the majority of these previously studied objects are biased toward AGN—two objects were previously identified in optical QSO surveys and 3 were selected on the basis of “warm” infrared colors, $f_{25}/f_{60} > 0.25$, which is known to preselect objects with AGN-like optical spectra (e.g. deGrijp et al. 1985). Therefore, to avoid biasing our 1-Jy sample classifications toward AGN, only the two BGS ULIGs out of the 7 previously classified objects (these two ULIGs are flagged with a dagger in Table 2) will be used in this paper for computing the distribution of spectral types (§4.1), and since new spectra were not obtained for any of the 7 previously classified ULIGs none of these 7 objects will be included in any other analyses.

Tables 3 and 4 list the various spectral parameters measured from our new data. Following Kim et al. (1995), the line fluxes were measured using two methods. The fluxes of isolated emission lines were measured using the standard plotting package in IRAF (“splot”), while “specfit”, an interactive spectral analysis procedure linked to IRAF and kindly provided by Gerard A. Kriss, was used to deal with blended lines (e.g., $\text{H}\alpha + [\text{N II}] \lambda\lambda 6548, 6583$ and $[\text{S II}] \lambda\lambda 6716, 6731$) and emission lines affected by stellar absorption features (e.g. $\text{H}\beta$ and $\text{H}\alpha$). This last routine can fit a wide variety of emission-line, absorption-line, and continuum models to the observed spectrum. The input parameters for the fit were determined through “splot” in IRAF. We chose to fit the continuum with a simple first-order polynomial, and the emission and absorption lines with Gaussian profiles. The actual fitting was done via a chi-square minimization using a simplex algorithm. The output parameters were the flux level and slope of the underlying continuum emission, the flux, centroid, and full-width-half-maximum (FWHM) of the emission lines, and equivalent width (EW), centroid, and FWHM of the absorption lines. All of the EWs discussed in this paper were derived in the object rest frame.

4. Results from the Analysis of the Nuclear Data

4.1. Spectral Classification

All of the ULIGs in our current study present a spectrum with emission lines. The characteristics of these lines are important indicators of the physical conditions of the thermal gas in our sample galaxies. In an attempt to determine the dominant source of ionization in these objects, four diagnostic line ratios known to be efficient at differentiating between the various ionization mechanisms (Veilleux & Osterbrock 1987; hereafter VO87) were used. These are [O III] $\lambda 5007/H\beta$, [N II] $\lambda 6583/H\alpha$, [S II] $\lambda\lambda 6716, 6731/H\alpha$, and [O I] $\lambda 6300/H\alpha$. All of the line ratios used in the present analysis have been corrected for reddening using the values of $E(B-V)$ determined from the $H\alpha/H\beta$ ratio and the Whitford reddening curve as parameterized by Miller & Mathews (1972; see next section).

The measurements are listed in Table 5 and are plotted in Figure 2. For each object in Table 5, entries on the first row represent the observed line ratios, while the second row lists the dereddened line ratios. Columns (8), (9), and (10) list the spectral types determined from the location of the data points in the diagrams of [O III] $\lambda 5007/H\beta$ versus [N II] $\lambda 6583/H\alpha$, [S II] $\lambda\lambda 6716, 6731/H\alpha$, and [O I] $\lambda 6300/H\alpha$, respectively. The boundaries of VO87 were used to classify each object as H II or AGN-like galaxies. A distinction was made among AGN-like galaxies between the objects of high ([O III] $\lambda 5007/H\beta \geq 3$) and low ([O III] $\lambda 5007/H\beta \leq 3$) excitation. The first group represents the “classic” Seyfert 2 galaxies while galaxies in the second group were classified as LINERs (“low-ionization nuclear emitting regions”), although a few of them may not satisfy the original LINER definition of Heckman (1980). Finally, column (11) of Table 5 gives the adopted spectral type based on the previous three columns. Galaxies with Fe II multiplets at $\lambda\lambda 5100-5560$ and very broad ($\Delta V_{\text{FWHM}} \gtrsim 1000 \text{ km s}^{-1}$) H I Balmer and He I $\lambda 5876$ emission lines were classified as Seyfert 1s. Eight systems in our sample appear double. In FSC 08572+3915 (LINER, LINER), FSC 14348-1447 (LINER, LINER), FSC 16468+5200 (LINER, LINER), and FSC 17028+5817 (LINER, H II), a LINER classification was adopted for the whole system, while in FSC 14202+2615 (H II, main nucleus), FSC 14394+5332 (Seyfert 2, western nucleus), FSC 16333+4630 (LINER, western main nucleus), and FSC 18470+3233 (H II, main component on the south-west), only the spectrum of the main component was available, and therefore the spectral type of that component was adopted for these systems.

Out of the 47 ULIGs that make up our unbiased infrared selected sample (i.e. all sources in Table 2 except the 5 sources identified in previous optically selected AGN catalogs), 28% of them (13/47) were found to have spectra characteristic of photoionization by hot stars (H II region-like). AGN-like emission lines were observed in 72% (34/47) of the total sample including 13% (6/47) Seyfert 1s, 21% (10/47) Seyfert 2s, and 38% (18/47) LINER-like objects. These results were combined with the measurements obtained by VKSMS for the LIGs from the BGS to search for systematic variations of the spectral types with infrared luminosity. For this exercise, ULIGs were further divided into two luminosity bins: $10^{12} L_{\odot} \leq L_{\text{ir}} < 10^{12.3} L_{\odot}$ and $L_{\text{ir}} \geq 10^{12.3} L_{\odot}$.

A summary of this analysis is given in Table 6 and plotted in Figure 3. There is an obvious tendency for the more luminous objects to have AGN-like line ratios and for these objects to be more Seyfert-like. In fact, none of the Seyfert 1 galaxies have $L_{\text{ir}} < 10^{11} L_{\odot}$ and about half of the galaxies with $L_{\text{ir}} \geq 10^{12.3} L_{\odot}$ present Seyfert characteristics.

LINER-like galaxies constitute 30–40% of the total sample regardless of L_{ir} . Essentially all of the ULIGs in our sample classified as H II galaxies have relatively low ionization level ($[\text{O III}] \lambda 5007/\text{H}\beta < 3$) and fall outside of the region populated by galaxies with very recent bursts of star formation (Evans & Dopita 1985; McCall, Rybski, & Shields 1985; Allen et al. 1991). The only galaxy that lies anywhere near this region of the $[\text{O III}]/\text{H}\beta$ vs. $[\text{N II}]/\text{H}\alpha$ diagram is FSC 15206+3342. This general lack of high-excitation H II galaxies among LIGs was also observed in the samples of VKSMS, Leech et al. (1989), Armus et al. (1989), Allen et al. (1991), Ashby, Houck, & Hacking (1992), and Ashby et al. (1995). The lack of Wolf-Rayet features in our sample galaxies also argues against a very recent burst ($\ll 10^7$ yr) of star formation.

As indicated in the reference column of Table 2, seven galaxies from the sample of VKSMS have also been observed in the present study. The spectral types derived from these two sets of data agree for all but two of these objects: FSC 13428+5606 (now classified as a Seyfert 2 galaxy rather than a LINER) and FSC 15327+2340 (now classified as a LINER instead of a Seyfert 2 galaxy). The different classification of the first object is due to a slight change in the $[\text{O III}] \lambda 5007/\text{H}\beta$ ratio which may be attributable to differences in the sizes of the extraction apertures used for these data. The present data were extracted from the central 4 kpc diameter region of this galaxy while VKSMS used a 2 kpc aperture. The difference in the spectral type of FSC 15327+2340 is probably due to the rather poor quality of the original VKSMS data on this object compounded with centering errors more likely to affect the older data. For both of these galaxies, the spectral type derived from the present data will be used in the following discussion.

4.2. Reddening

The reddening in our sample galaxies was estimated using the emission-line $\text{H}\alpha/\text{H}\beta$ ratios corrected for the underlying stellar absorption features. An intrinsic $\text{H}\alpha/\text{H}\beta$ ratio of 2.85 was adopted for H II region-like galaxies (Case B Balmer recombination decrement for $T = 10^4$ K and $n_e = 10^4 \text{ cm}^{-3}$) and 3.10 for AGN-like galaxies (see references in VO87). The Whitford reddening curve as parameterized by Miller & Mathews (1972) was used. The reddenings derived from this method are listed as color excesses, $E(B-V)$, in the third column of Table 5. Since nearly all the objects in our sample lie at $|b| > 30^\circ$, no correction was made for Galactic reddening. Note that the extinction measurements based on the optical spectra are likely to represent lower limits to the true extinction because the observed line and continuum emission from an inhomogeneous environment like that of the nuclear regions of ULIGs will come predominantly from regions of smaller optical depths.

The distribution of $E(B-V)$ for the ULIGs of our sample is shown in Figure 4. The median $E(B-V)$ are 1.13, 1.02 and 1.54 for H II galaxies, LINERs and Seyfert 2 galaxies, respectively. Kolmogorov-Smirnov (K-S) tests indicate that the differences between the various spectral types are not significant. These color excesses are similar to those obtained by VKSMS in the lower-luminosity galaxies of the BGS [$E(B-V) = 1.05, 1.24, \text{ and } 1.07$ for H II galaxies, LINERs, and Seyfert 2 galaxies, respectively]. However, VKSMS found that the color excesses of the LINERs were significantly larger than those of the H II and Seyfert 2 galaxies. The color excesses measured in the ULIGs of our sample and the lower luminosity objects of VKSMS are considerably larger than those measured in optically-selected Seyfert and starburst galaxies (Dahari & De Robertis 1988) and in extragalactic H II regions (Kennicutt, Keel, & Blaha 1989). These results confirm the importance of dust in infrared galaxies, regardless of their infrared luminosity.

The correlation observed by VKSMS between $E(B-V)$ and $EW(\text{NaId})$ of H II galaxies is also present, but perhaps at a weaker level, among our high-luminosity objects (Fig. 5). The probabilities, $P[\text{null}]$, that these correlations are fortuitous are 3×10^{-4} , 0.07, and 0.10 among the H II galaxies, LINERs, and Seyfert 2 galaxies of the combined sample. Figure 6 shows that a similar correlation is observed between $E(B-V)$ and the observed continuum colors of H II galaxies ($P[\text{null}] = 2 \times 10^{-11}$) and, to a lesser extent, LINERs ($P[\text{null}] = 2 \times 10^{-4}$), but not among the Seyfert 2 galaxies ($P[\text{null}] = 0.78$). As first reported by VKSMS, these results suggest that the scatter in the Na Id equivalent widths and continuum colors of the Seyfert LIGs is predominantly intrinsic rather than caused by variations in the amount of reddening from one object to the other.

4.3. Densities

Figure 7 shows the distribution of the electron densities as a function of spectral type. K-S tests indicate that these distributions are not significantly different. The median values of the electron densities, n_e , are 170 cm^{-3} , 140 cm^{-3} , and 280 cm^{-3} for H II region galaxies, LINERs and Seyfert 2 galaxies, respectively. These median densities are comparable to those obtained by VKSMS for the lower luminosity infrared galaxies, but are considerably smaller than those found by Koski (1978) and Keel (1983) in optically-selected LINERs, Seyfert 2 and narrow-line radio galaxies. A possible explanation for this difference is that the strong dust extinction in infrared-selected galaxies prevents us from probing the inner, presumably denser [S II] line-emitting zone in these objects (see VKSMS).

4.4. Line Widths

[O III] $\lambda 5007$ was selected for line width measurements because it is strong in most ULIGs and free of any nearby emission or absorption lines (in contrast to $\text{H}\alpha$). The line widths listed in Table 4 have been corrected for the finite instrument resolution of the data ($\sim 8 \text{ \AA}$) using the

quadrature method. This method assumes that the intrinsic and instrument profiles are Gaussian and gives corrected widths that are too large for profiles which are more peaky than Gaussians (e.g., the emission-line profiles in AGN; Whittle 1985; Veilleux 1991). For this reason, the [O III] $\lambda 5007$ line widths should be treated with caution.

Figure 8 shows the distribution of the [O III] line widths for each spectral type. The median line widths, ΔV_{FWHM} , of the H II galaxies and LINERs are comparable (170 km s^{-1} and 130 km s^{-1}) whereas the [O III] line widths of Seyfert 2 galaxies appear larger (500 km s^{-1}). K-S tests indicate, however, that the differences are not particularly significant because of the small number of galaxies in each category. The probability that the line widths of H II galaxies and LINERs are drawn from the same population is 0.40, it is 0.04 when comparing the line widths of H II and Seyfert 2 galaxies, and 0.10 for the LINERs and Seyfert 2 galaxies. In comparison, VKSMS derived median line widths of 255, 310, and 350 km s^{-1} for the H II, LINER, and Seyfert 2 LIGs of the BGS. A K-S comparison of these results with those that were obtained for our ULIGs show that they are not statistically very different.

Based on the existence of objects with very broad and complex line profiles in their sample, VKSMS argued that the line broadening in some LIGs (particularly those with AGN-like spectral features) is caused in part by non-gravitational processes associated with nuclear outflows. Figure 9 illustrates the distribution of [O III] line widths of the combined sample as a function of infrared luminosity. It is interesting to note that all the objects with line widths larger than 600 km s^{-1} have $L_{\text{ir}} \gtrsim 10^{11} L_{\odot}$, and objects with the most extreme profiles ($\Delta V_{\text{FWHM}} > 1000 \text{ km s}^{-1}$) all have $L_{\text{ir}} > 10^{12} L_{\odot}$ and Seyfert characteristics. When the line widths measured in both samples are plotted as a function of the *IRAS* flux density ratio f_{25}/f_{60} , a well-known indicator of Seyfert activity in infrared galaxies (e.g., deGrijp et al. 1985; Miley, Neugebauer & Soifer 1985), a significant correlation is found among Seyfert 2 galaxies ($P[\text{null}] = 0.01$) but none among H II galaxies ($P[\text{null}] = 0.36$) or LINERs ($P[\text{null}] = 0.22$). These results (see Figure 10) suggest that the nuclear activity in the Seyfert ULIGs may contribute to the line broadening.

4.5. Stellar Absorption Features

The distributions of the equivalent widths of $\text{H}\beta$ and Mg Ib are presented in Figures 11 and 12. Unfortunately, our spectra do not extend far enough in wavelengths to cover the important Ca II triplet feature (see VKSMS). The median $EW(\text{H}\beta)$ for our ULIGs are 0.77 \AA , 0.84 \AA , and 0.41 \AA for the H II galaxies, LINERs, and Seyfert 2 galaxies, respectively. The small number of Seyfert galaxies with accurately measured $\text{H}\beta$ makes the apparently smaller equivalent width of these objects uncertain. K-S tests indicate, however, that these equivalent widths are significantly smaller than those measured by VKSMS in the BGS LIGs (2.28 \AA , 2.18 \AA , and 2.49 \AA , respectively; $P[\text{null}] = 0.03, 0.4, 0.005$, respectively). The intermediate-age (10^8 – 10^9 yr) population of stars that is responsible for the $\text{H}\beta$ absorption feature is less prominent in our sample of ULIGs. A possibility is that the $\text{H}\beta$ feature is being diluted by a hot, featureless continuum from young stars

(particularly in H II galaxies) or from an AGN (in Seyfert 2 galaxies).

In this context, it is not surprising to find that the $EW(\text{Mg Ib})$ for our sample of ULIGs (median values of 1.1 Å, 1.4 Å, and 0.7 Å for H II galaxies, LINERs, and Seyfert 2 galaxies, respectively) are considerably smaller than those measured in non-active spiral galaxies [$EW(\text{Mg Ib}) = 3.5\text{--}5.0$ Å: Keel 1983; Stauffer 1982; Heckman, Balick, & Crane 1980]. However, these values are *not* significantly different from those measured in the BGS objects of VKSMS (1.12 Å, 1.49 Å, and 1.17 Å, respectively). Consequently, the stellar population of LIGs *and* ULIGs is probably not old enough ($> 10^9$ yr; Bica, Alloin, & Schmidt 1990) to produce strong $EW(\text{Mg Ib})$. Any featureless continuum from young stars or from an AGN would also weaken the spectral signatures of the underlying old stellar population. This issue will be discussed further when the radial behavior of these spectral features in the sample galaxies is presented (§5.4).

4.6. Continuum Colors

The observed continuum colors were dereddened using the amount of dust derived from the emission-line spectrum. The results are presented in Figure 13. The dereddened continuum colors of the Seyfert 2 ULIGs may be slightly bluer on average than those of the H II galaxies and LINERs but the difference is not statistically significant (median $[C6563/C4861]_0 = 0.39, 0.39,$ and $0.22,$ for H II galaxies, LINERs, and Seyfert 2 galaxies, respectively). In Figure 14 shows a strong anti-correlation between the dereddened continuum colors and $H\alpha$ luminosities in the combined sample of LIGs ($P[\text{null}] = 2 \times 10^{-6}, 9 \times 10^{-5},$ and 0.005 for the H II galaxies, LINERs, and Seyfert 2 galaxies, respectively). Interestingly, this anti-correlation virtually disappears ($P[\text{null}] \gtrsim 0.01$) when the infrared luminosities are used instead of the $H\alpha$ luminosities (Figs. 15), suggesting that the driving parameter that determines the optical continuum color in these galaxies is the luminosity that emerges from the nucleus at optical wavelengths rather than the total energy output. The anti-correlation observed in Figure 14 may also be an artifact of our assumption that the continuum emission is reddened by the same amount as the emission lines. Although it is unlikely that the amount of reddening in the emission-line gas has been overestimated (§4.2), the same may not be true of the continuum source. Indeed, the inverse correlation shown in Figure 14 could result if the ionized gas is more strongly concentrated than the continuum source (in which case the dereddened continuum would be overcorrected for reddening and therefore too blue), and if the relative concentration of the ionized gas increases with increasing emission-line luminosity.

Assuming that most of the optical continuum of our H II and LINER ULIGs is produced by the underlying stellar population and using the continuum colors of the stellar cluster models of Jacoby, Hunter, & Christian (1984), the underlying optical continuum in these objects appears to be dominated by a young stellar population characterized by a starburst age of $\sim 10^7$ years. A similar result was derived from the samples of VKSMS and Armus et al. (1989). The slightly bluer continuum of the Seyfert 2 ULIGs, though only marginally significant, may indicate the presence of an additional source of activity in these objects.

4.7. H α Luminosities and Equivalent Widths

The distributions of H α equivalent widths and reddening-corrected H α luminosities are plotted in Figures 16 and 17 for each spectral type. The median $\{\log[EW(\text{H}\alpha) \text{ \AA}], \log(L_{\text{H}\alpha}/L_{\odot})_0\}$ are $\{2.1, 9.0\}$, $\{1.8, 8.7\}$, and $\{1.9, 9.6\}$ for HII galaxies, LINERs, and Seyfert 2 galaxies, respectively. Both sets of measurements seem to indicate that LINER ULIGs are slightly deficient in H α relative to HII and Seyfert 2 ULIGs. A similar result was found by VKSMS in the lower luminosity objects. Rigorous K-S tests indicate, however, that the differences between the various types of ULIGs are only marginally significant.

A strong correlation is found between H α and infrared luminosities (Fig. 18; $P[\text{null}] = 4 \times 10^{-8}$, 1×10^{-7} , and 0.005 for the HII galaxies, LINERs and Seyfert 2 galaxies in the combined sample, respectively). Slightly weaker correlations are observed when the H α luminosities are replaced by the H α equivalent widths (Fig. 19; $P[\text{null}] = 3 \times 10^{-6}$, 6×10^{-8} , and 0.26, respectively). The infrared-to-H α luminosity ratios in Seyfert 2 ULIGs are slightly smaller than those of HII and LINER ULIGs but the difference is not statistically significant [median $\log(L_{\text{ir}}/L_{\text{H}\alpha}) = 3.11, 3.47, 3.05$ for the HII, LINER, and Seyfert 2 ULIGs, respectively]. The presence of an additional, non-stellar source of energy in some of the Seyfert ULIGs may result in infrared-to-H α luminosity ratios that differ from the nominal value of starburst-powered galaxies embedded in dust.

If the HII and LINER ULIGs of our sample are purely powered by stars, both the infrared and H α luminosities can be used to estimate the rate of star formation in these galaxies. Using equations (1) and (2) of VKSMS, prodigious star formation rates of $\sim 250\text{--}1,000 \beta^{-1} M_{\odot} \text{ yr}^{-1}$ are derived based on the infrared luminosities and $\sim 1\text{--}250 \eta^{-1} M_{\odot} \text{ yr}^{-1}$ based on their *nuclear* H α luminosities. The parameters β and η in these rates are the fraction of the bolometric luminosity radiated by stars and the fraction of ionizing photons that produce observable H α emission, respectively. The difference between these star formation rates is probably due in most part to the fact that the H α -based rates refer only to the nuclei while the infrared-based rates take into account the star formation in both the nuclear and circumnuclear regions.

Little is known about the masses of molecular gas in the ULIGs of our sample. Therefore, the depletion time scales in these objects are difficult to estimate. Sanders, Scoville, & Soifer (1991) found that the infrared luminosity-to-H $_2$ mass ratios for ~ 60 BGS galaxies increase roughly linearly with increasing L_{ir} . If this relation also applies to the ULIGs studied in this paper and if the observed L_{ir} is powered entirely by star formation, the star formation rates derived for these galaxies (e.g. Sanders et al. 1991) will transform the entire interstellar medium into massive stars in only about $4 \times 10^7 L_{\text{ir},12}^{-1} \text{ yr}$ (neglecting the mass loss of these stars back into the interstellar medium and assuming no low-mass stars are formed). This timescale is shorter than the lifetime of the ultraluminous phase estimated by Carico et al. (1990) from the frequency of double nuclei in these systems. The time scale for gas depletion may be underestimated if the ULIGs are anomalously rich in molecular gas (relative to their infrared luminosity) or if the initial mass function is skewed towards massive stars (e.g., Rieke et al. 1993).

5. Spatial Information

The previous section presented the spectral properties of the nuclear regions ($R < 2$ kpc) of our sample galaxies. This section discusses the behavior of these properties as a function of the distance from the nucleus. The line emission in our sample galaxies often peaks in the nuclear region. Consequently, in order to maximize the signal-to-noise ratio in each radial bin, we used extraction windows with sizes that gradually increase with radial distance from the nucleus. Two methods of extraction were used. In both cases, a central portion of the galaxy was first extracted from the long-slit spectra, corresponding roughly to the size of the seeing disk ($R = 1$ kpc for objects with $z < 0.15$ and $R = 2$ kpc for the other galaxies). To study the effects of aperture size on the spectral classification of our sample galaxies, extraction windows were used that covered the following radial bins: 0–1 kpc (exclusively for the objects with $z < 0.15$), 0–2 kpc, 0–4 kpc, and 0–8 kpc (for the few objects with $z > 0.15$). To determine the radial behavior of the spectral parameters, the nuclear portion of the galaxy was extracted first, followed by extracted portions of the spectrum on both sides of the nucleus. The size of the extraction windows was increased gradually at larger distances from the nucleus. For this second method, the extraction windows used for the low-redshift objects covered $R = 0$ –1 kpc (data points at $R = 0.5$ kpc in the figures), $R = 1$ –2 kpc (data points at $R = 1.5$ kpc), and $R = 2$ –4 kpc (data points at $R = 3$ kpc). For the objects with $z > 0.15$, the extraction windows covered $R = 0$ –2 kpc (data points at $R = 1$ kpc in the figures), 2–4 kpc (data points at $R = 3$ kpc), and $R = 4$ –8 kpc (data points at $R = 6$ kpc). It proved possible to carry out this analysis for 34 objects in our sample. These galaxies are indicated by an asterisk (*) in Table 2.

A summary of the results is presented in Table 7 and in Figures 20–22. This last figure deserves further explanations: to attempt to detect any systematic differences between the various spectral types, we plotted in Figure 22 the mean spectral parameters of each spectral type, with the error bars in this figure indicating the standard deviations from the means in each radial bin. For this exercise, the mean of the spectral parameters were selected for the following radial bins: 0–1 kpc, 1–2 kpc, 2–4 kpc, and 4–8 kpc. This technique therefore results in the loss of some data because it does not take into account the nuclear parameters of the high-redshift galaxies extracted over $R = 0$ –2 kpc. Moreover, one should note that the radial bins 0–1 kpc and 4–8 kpc are covered only by the low and high-redshift objects, respectively. Nevertheless, we believe that Figure 22 is a powerful tool for summarizing our results.

5.1. Spectral Classification

Figure 20 shows the variations of the line ratios as a function of aperture size. The spectral types of $\sim 20\%$ of the ULIGs are found to depend on the size of the aperture (6, 7, and 5 objects in the diagrams involving $[\text{O I}]/\text{H}\alpha$, $[\text{S II}]/\text{H}\alpha$, and $[\text{N II}]/\text{H}\alpha$ plots, respectively). A similar fraction ($\sim 25\%$) of the VKSMS sample of LIGs was found to change spectral type with aperture size.

Once again, this result emphasizes the fact that a constant linear-size aperture is crucial when comparing the nuclear emission-line spectra of LIGs having different redshifts.

Dramatic radial variations of the line ratios are observed in several of the galaxies (Fig. 21). In particular, an important fraction of the galaxies with nuclear H II characteristics harbor distinct AGN-like line ratios (generally LINER-like but in some cases even Seyfert-like) at larger distances from the nucleus (5, 8, and 3 objects in the [O I]/H α , [S II]/H α , and [N II]/H α plots, respectively). This behavior was also observed in a few objects from the sample of VKSMS. This result was interpreted by VKSMS in the context of supernova-driven wind models in which the circumnuclear gas is collisionally ionized by strong shocks caused by the interaction of the outflowing nuclear gas with the ambient material (e.g., M 82; Heckman, Armus, & Miley 1990). The broad [O III] line widths observed outside the nuclei of many H II ULIGs (Fig. 22) brings support to this idea. Shocks may also explain the Seyfert-like line ratios observed in a few cases (e.g., Binette, Dopita, & Tuohy 1985; Dopita & Sutherland 1995).

A careful inspection of Figure 21 reveals that the level of ionization of most galaxies with nuclear Seyfert 2 spectra tends to decrease at larger radii. The [O III]/H β ratios of these objects are often lower outside of the nucleus and [O I]/H α , [S II]/H α , and [N II]/H α often increase with radius. A direct comparison of these results with the line ratios predicted by photoionization models (e.g., Ferland & Netzer 1983; VO87) suggests that the ionization parameter (\equiv density of ionizing photons/hydrogen density) is decreasing away from the nucleus of these galaxies, as expected if the source of ionization is a point source such as an AGN and if the density profile is not a steeply decreasing function of distance from the nucleus. Circumnuclear starbursts may also contribute in some cases to dilute the AGN emission and decrease the degree of ionization of the gas surrounding the AGN.

5.2. Reddening

The radial variations of $E(B-V)$ derived from H α /H β are presented in Figure 22a. For simplicity, it was assumed that the intrinsic Balmer decrements outside of the nucleus is the same as in the nucleus [i.e., it was assumed $(H\alpha/H\beta)_0 = 2.85$ in and out of the H II nuclei and 3.1 in and out of the AGN-like nuclei]. No significant differences are observed between the mean reddening profiles of the various spectral types (Fig. 22a). The color excess shows a general tendency to decrease with radius. However, there is substantial scatter around the mean profile of each spectral type. In at least 4 and possibly 7 galaxies (FSC 10494+4424, FSC 14378-3615, FSC 16333+4630, FSC 17208-0014; FSC 11582+3020, FSC 16468+5200, FSC 17044+6720), the amount of reddening appears to peak outside of the nucleus. Six of these galaxies present a LINER-like nuclear spectrum. This fraction of galaxies with inverted reddening profiles is qualitatively similar to that found by VKSMS in the LIGs: 2 LINERs and 1 Seyfert 2 galaxy among the 23 LIGs. It is not clear at present whether inverted reddening profiles reflect the actual dust distribution in these objects or whether they are caused by complex optical depth effects. High-resolution ($\lesssim 1''$)

observations of our 1-Jy galaxies at millimeter wavelengths could prove useful for determining how the molecular gas is distributed in these ULIGs.

5.3. Line Widths

The radial variations of the [O III] line widths are presented in Figure 22b. We note that the Seyfert 2 ULIGs present [O III] profiles that are broader than those of H II and LINER ULIGs not only in the nucleus (§4.4) but also out to radii of $\sim 2\text{--}3$ kpc. The large line widths in the circumnuclear regions of the Seyfert 2 ULIGs suggest that the gas near the nucleus is feeling the dynamical effects of the AGN presumed to exist in these objects. This process is known to take place in a number of optically-selected Seyfert galaxies (e.g., Whittle 1994).

It is harder to explain the apparent tendency for the [O III] profiles in H II and LINER ULIGs to be broader *outside* of the nucleus. One possibility — proposed by VKSMS to explain their own data — is that the broad line profiles outside of the nuclei of these objects are produced by (unresolved) line splitting where two or more kinematic components with different velocities are present. Extra-nuclear line splitting due to nuclear outflows is a relatively common feature in the handful of LIGs for which high-resolution kinematic data exist in the literature (e.g., Bland & Tully 1988; Heckman, Armus, & Miley 1990; Veilleux et al. 1994 and references therein). It is possible that this process is taking place in some of our sample galaxies (see §5.1), but this process may have difficulties explaining the fact that the line widths of an important fraction of the H II and LINER galaxies are *monotonically* increasing outward from the nucleus. Another possible source of broadening is galactic rotation. The importance of this effect is a complex function of the rotation curve, the distribution of the line emission, and the size of the aperture. Under certain conditions, the radially increasing size of our extraction apertures may indeed result in line smearing/broadening that could reproduce the observations. Unfortunately, the spectral resolution of the present data is not sufficient to answer this question. Finally, we cannot completely rule out the possibility that the measurements obtained outside of the nuclei are affected by numerical broadening associated with Poisson noise (noisier signals tend to pull in more of the emission in the wings away from the peak and so broaden the fitted line profile). Data of higher signal-to-noise ratios and spectral resolution would settle this controversy unambiguously.

5.4. Stellar Absorption Features, Continuum Colors and $H\alpha$ Luminosities

The radial behavior of the $H\beta$ and Mg Ib equivalent widths are plotted in Figures 22c and 22d. The strength of both features is relatively constant with radius. The Mg Ib feature *at all radii* is generally weaker than that of non-active spiral galaxies [$EW(\text{Mg Ib}) = 3.5\text{--}5.0 \text{ \AA}$: Keel 1983; Stauffer 1982; Heckman, Balick, & Crane 1980]. The strength of the $H\beta$ feature, on the other hand, covers a range that is similar to that of non-active spiral galaxies ($\sim 1.4 \text{ \AA}$: Keel

1983). It is hard to simply invoke dilution effects by a featureless continuum from hot stars to explain both sets of results simultaneously and at all radii. A natural explanation of these radial behaviors is that the old (Mg Ib-producing) stellar population present in non-active galaxies is less prominent in ULIGs. Dilution effects probably become an important factor in the nucleus, however (especially in Seyfert 2 galaxies; see §4.5 and below).

Figure 22e presents the radial variations of the reddening-corrected continuum colors. Irrespective of spectral types, the median values of $(C6563/C4861)_0$ in ULIGs are ~ 0.4 within $R = 0-3$ kpc. The estimated age of the underlying stellar population with these continuum colors is $\sim 10^7$ years (Jacoby et al. 1984; VKSMS).

None of the apparent differences between spectral types (Fig. 22c, 22d, and 22e) are statistically significant. However, the slightly smaller *nuclear* values of $EW(H\beta)$, $EW(Mg Ib)$, and $(C6563/C4861)_0$ in the Seyfert 2 ULIGs are consistent with the presence of an additional source of activity in the nuclei of these objects. The nuclear peak of the $H\alpha$ emission in Seyfert galaxies (Fig. 22f) — in spite of the fact that the size of the extraction windows increases with radius — confirms that the activity in these objects is more highly concentrated in the nucleus than in any other classes of ULIGs. The peak is slightly less pronounced when $L_{H\alpha}$ is replaced by $EW(H\alpha)$ (see Fig. 22g).

6. Summary

An optical spectroscopic study of the nuclear regions of an unbiased subsample of 45 ultraluminous infrared galaxies from Paper I, has been completed. The spectral properties of the circumnuclear regions in 34 of these objects were also examined. These data were then combined with our results from a previous study of primarily lower luminosity infrared galaxies (VKSMS) to examine the spectra properties of LIGs over the range $L_{ir} \approx 10^{10.5} - 10^{12.9} L_{\odot}$. The main conclusions of this analysis are the following:

1. The fraction of LIGs with Seyfert characteristics continues to increase with increasing L_{ir} . For $L_{ir} > 10^{12.3} L_{\odot}$, about 45% of the ULIGs (9/20 objects) are classified as Seyfert 1s or 2s.
2. Many properties of the Seyfert galaxies in our sample suggest the presence of a nuclear source of activity in these objects that is absent or not visible in H II galaxies or LINERs. The distribution of the $H\alpha$ emission in Seyfert galaxies is more centrally peaked than in H II galaxies and LINERs. The nuclei of Seyfert galaxies present a slightly bluer continuum and weaker stellar features. The line widths within $R \sim 2 - 3$ kpc of the nuclei of Seyfert galaxies are broader on average than those measured in the H II and LINER ULIGs. The variations of the line ratios in Seyfert galaxies imply that the ionization parameter is decreasing away from the nucleus of many of these galaxies, as expected if the source of ionization is a point source like an AGN.

3. In contrast, the LINER ULIGs share more often than not the properties of H II galaxies, and therefore may not be genuine AGN. In some cases, the radial variations of the line ratios suggest that the extranuclear LINER-like emission is produced through shocks caused by the interaction of starburst-driven outflows with the ambient material. Note that this statement only refers to the infrared-selected LINERs of our sample, and may not necessarily apply to optically-selected LINERs.
4. The continuum colors and strengths of the stellar $H\beta$ and $Mg\text{Ib}$ features in and out of the nuclei of ULIGs indicate that a young ($\sim 10^7$ year) stellar population is present at all radii and overwhelms the emission from the old, underlying stellar population in these objects. Star formation rates of $\sim 250\text{--}1,000 M_{\odot} \text{ yr}^{-1}$ and $\sim 1\text{--}250 M_{\odot} \text{ yr}^{-1}$ are derived from the *total* infrared luminosities and *nuclear* $H\alpha$ luminosities, respectively. These prodigious star formation rates will transform the entire interstellar medium into massive stars in only a few $\times 10^7$ yr unless these galaxies are anomalously rich in molecular gas (relative to their infrared luminosity) or if the initial mass function is skewed towards massive stars.
5. Based on the color excesses derived from the $H\alpha/H\beta$ emission-line ratios, the importance of dust in the nuclei of ULIGs appears comparable to that measured in the *IRAS* galaxies of lower infrared luminosities. However, in contrast to what was found in low-luminosity infrared galaxies, the color excess in the nuclei of ULIGs does not seem to depend on spectral types. The reddening in both the high and low luminosity objects is generally observed to decrease with distance from the nucleus. Clear cases of inverted reddening profiles are observed in less than 1/5 of the ULIGs in our sample, nearly all of which are optically classified as LINERs. Complex optical depth effects may distort our view of the dust distribution in these objects, and make the interpretation of these inverted reddening profiles difficult. High-resolution observations of these objects at millimeter/submillimeter wavelengths would clarify this issue.

Optical spectra of the remaining objects in the 1-Jy sample have been collected and are presently being analyzed (Veilleux et al. 1997a). An analysis of near-infrared spectra on a representative subset of 25 objects from the 1-Jy sample was also recently presented (Veilleux, Sanders, & Kim 1997b). These data will be combined together into a large optical/near-infrared data base that will allow us to make firmer statements on the statistical significance of the results discussed in the present paper.

The IRAF procedure “specfit” was developed and kindly provided by Gerard A. Kriss with funding by NASA to the Hopkins Ultraviolet Telescope project. This research was supported in part by NASA grants NAG5-1251 and NAG5-1741 to the University of Hawaii (D. B. S. and D.-C. K.). S. V. gratefully acknowledges the financial support of NASA through grant number HF-1039.01-92A awarded by the Space Telescope Science Institute which is operated by the AURA, Inc. for NASA under contract No. NAS5-26555. This research has made use of the

NASA/IPAC Extragalactic Database (NED) which is operated by the Jet Propulsion Laboratory, California Institute of Technology, under contract with NASA.

REFERENCES

- Allen, D. A., Norris, R. P., Meadows, V. S., & Roche, P. F. 1991, *MNRAS*, 248, 528
- Armus, L., Heckman, T. M., & Miley, G. K. 1989, *ApJ*, 347, 727
- Ashby, M., Houck, J. R., & Hacking, P. B. 1992, *AJ*, 10, 980
- Ashby, M., Houck, J. R., & Matthews, K. 1995, *ApJ*, 447, 545
- Bica, E., Alloin, D., & Schmidt, A. 1990, *MNRAS*, 242, 241
- Binette, L., Dopita, M. A., & Tuohy, I. R. 1985, *ApJ*, 297, 476
- Bland, J., & Tully, R. B. 1988, *Nature*, 334, 43
- Carico, D. P., Graham, J. R., Matthews, K., Wilson, T. D., Soifer, B. T., Neugebauer, G., & Sanders, D. B. 1990, *ApJ*, 349, L39
- Dahari, O., & De Robertis, M. M. 1988, *ApJS*, 67, 249
- de Grijp, M. H. K., Miley, G. K., Lub, J., & De Jong, T. 1985, *Nature*, 314, 240
- De Robertis, M. M., Dufour, R. J., & Hunt, R. W. 1987, *JRASC*, 81, 195
- Dopita, M. A., & Sutherland, R. S. 1995, *ApJ*, 455, 468
- Elston, R., Cornell, M. E., & Lebofsky, M. J. 1985, *ApJ*, 296, 106
- Evans, I. N., & Dopita, M. A. 1985, *ApJS*, 57, 503
- Ferland, G. J., & Netzer, H. 1983, *ApJ*, 264, 105
- Heckman, T. M. 1980, *A&A*, 87, 152
- Heckman, T. M., Balick, B., & Crane, P. C. 1980, *A&AS*, 40, 295
- Heckman, T. M., Armus, L., & Miley, G. K. 1990, *ApJS*, 74, 833
- Hill, G. J., Heasley, J. N., Becklin, E. E., & Wynn-Williams, C. G. 1988, *AJ*, 95, 1031
- Jacoby, G. H., Hunter, D. A., & Christian, C. A. 1984, *ApJS*, 56, 256
- Keel, W. C. 1983, *ApJ*, 269, 466
- Kennicutt, R. C. Jr., Keel, W. C., & Blaha, C. A. 1989, *AJ*, 97, 1022
- Kim, D.-C. 1995, Ph. D. Thesis, University of Hawaii
- Kim, D.-C., & Sanders, D. B. 1997, *ApJS*, submitted (Paper I)
- Kim, D.-C., Sanders, D. B., & Mazzarella, J. M. 1996, *ApJ*, in preparation (Paper III)
- Kim, D. -C., Veilleux, S., Sanders, D. B., Mazzarella, J. M., & Soifer, B. T. 1995, *ApJS*, 98, 129
- Koski, A. T. 1978, *ApJ*, 223, 56
- Leech, K. J., Penston, M. V., Terlvich, R., Lawrence, A., Rowan-Robinson, M. , & Crawford, J. 1989, *MNRAS*, 240, 349
- Low, F. J., Huchra, J. P., Kleinmann, S. G., & Cutri, R. M. 1988, *ApJ*, 327, L41

- Mackenty, J. W., & Stockton, A. 1984, *ApJ*, 283, 64
- McCall, M. L., Rybski, P. M., & Shields, G. A. 1985, *ApJS*, 57, 1
- Miley, G. K., Neugebauer, G., & Soifer, B. T. 1985, *ApJ*, 293, L11
- Miller, J. S., & Mathews, W. G. 1972, *ApJ*, 172, 593
- Moshir, M. et al. 1992, Explanatory Supplement to the *IRAS* Faint Source Survey, Version 2, JPL D-10015 8/92 (Pasadena: JPL) (FSC)
- Perault, M. 1987, PhD Thesis, University of Paris
- Rieke, G. H., Loken, K., Rieke, M. J., & Tamblyn, P. 1993, *ApJ*, 412, 99
- Sanders, D. B., & Mirabel, I. F. 1996, *ARA&A*, 34, 725
- Sanders, D. B., Scoville, N. Z., & Soifer, B. T. 1991, *ApJ*, 370, 158
- Sanders, D. B., Soifer, B. T., Elias, J. H., Madore, B. F., Matthews, K., Neugebauer, G., & Scoville, N. Z. 1988, *ApJ*, 325, 74
- Schmidt, M. 1963, *Nature*, 197, 1040
- Scoville, N. Z., Sargent, A. I., Sanders, D. B., & Soifer, B. T. 1991, *ApJ*, 366, L5
- Soifer, B. T., Boehmer, L., Neugebauer, G., & Sanders, D. B. 1989, *AJ*, 98, 766
- Soifer, B. T., & Neugebauer, G. 1991, *AJ*, 101, 354
- Soifer, B. T., Sanders, D. B., Madore, B., Neugebauer, G., Danielson, G. E., Elias, J. H., Persson, C. J., & Rice, W. L. 1987, *ApJ*, 320, 238
- Solomon, P. M., Downes, D., & Radford, S. J. E. 1992, *ApJ*, 387, L55
- Stauffer, J. R. 1982, *ApJS*, 50, 517
- Veilleux, S. 1991, *ApJS*, 75, 383
- Veilleux, S., Cecil, G., Bland-Hawthorn, J., Filippenko, A. V., & Sargent, W. L. W. 1994, *ApJ*, 433, 48
- Veilleux, S., Kim, D. -C., Sanders, D. B., Mazzarella, J. M., & Soifer, B. T. 1995, *ApJS*, 98, 171 (VKSMS)
- Veilleux, S., & Osterbrock, D. E. 1987, *ApJS*, 63, 295 (VO87)
- Veilleux, S., Kim, C.-C., & Sanders, D. B. 1997, in preparation
- Veilleux, S., Sanders, D. B., & Kim, D.-C. 1997, *ApJ*, 484, 92
- Whittle, M. 1985, *MNRAS*, 213, 1
- Whittle, M. 1994, in *Mass-Transfer Induced Activity in Galaxies*, ed. I. Shlosman, (Cambridge University Press: Cambridge), 63

FIGURE CAPTIONS

Fig. 1.— Optical spectra of the ULIGs in our sample — f_λ is plotted vs $\lambda_{\text{observed}}$. The units of the vertical axis are $10^{-15} \text{ erg s}^{-1} \text{ cm}^{-2} \text{ \AA}^{-1}$ while the wavelength scale is in \AA .

Fig. 2.— Dereddened flux ratios. The H II region-like galaxies (H) are located to the left of the solid curve while AGN-like objects are located on the right. AGN-like objects were further classified as Seyfert-like or LINER-like depending on whether or not $[\text{O III}]\lambda 5007/\text{H}\beta \geq 3$ (indicated by a solid horizontal segment). Seyfert 1 galaxies are not shown in the diagrams.

Fig. 3.— Summary of the results of the spectral classification as a function of the infrared luminosity. The results from the present paper were combined with those obtained by Veilleux et al. (1995) on LIGs in the BGS. The fraction of Seyferts increases with infrared luminosity.

Fig. 4.— Distribution of the color excesses as a function of spectral types for the ULIGs in the present sample (solid line) and the BGS LIGs of Veilleux et al. (1995; dashed line). Both classes of objects present large color excesses. The differences between the various types of ULIGs are not significant.

Fig. 5.— Color excesses as a function of the equivalent widths of $\text{Na I d } \lambda 5892$ for each spectral type. The stars are the H II galaxies, the open circles are the LINERs, and the filled circles are the Seyfert 2 galaxies. The large symbols are the ULIGs from the present sample and the small symbols are the BGS LIGs from Veilleux et al. (1995). A significant correlation is observed among H II galaxies.

Fig. 6.— Color excesses as a function of observed continuum colors for each spectral type. The meaning of the symbols is the same as in Fig. 5. A correlation is observed among H II galaxies and LINERs.

Fig. 7.— Distribution of the electron density as a function of the spectral types of the ULIGs in the present sample (solid line) and the BGS LIGs of Veilleux et al. (1995; dashed line). No luminosity or spectral type dependence is observed.

Fig. 8.— Distribution of the $[\text{O III}] \lambda 5007$ line widths as a function of the spectral types of the ULIGs in the present sample (solid line) and the BGS LIGs of Veilleux et al. (1995; dashed line). The median line widths of H II and LINER ULIGs are somewhat smaller than those of Seyfert 2 ULIGs, but the difference is not significant.

Fig. 9.— $[\text{O III}] \lambda 5007$ line widths as a function of the infrared luminosities. The meaning of the symbols is the same as in Fig. 5. The objects with large $[\text{O III}]$ line widths generally have large infrared luminosities and many of them have Seyfert characteristics.

Fig. 10.— [O III] $\lambda 5007$ line widths as a function of the flux density ratios f_{25}/f_{60} for each spectral type. The meaning of the symbols is the same as in Fig. 5. A correlation is observed among Seyfert 2 galaxies.

Fig. 11.— Distribution of the equivalent widths of H β in absorption as a function of the spectral types of the ULIGs in the present sample (solid line) and the BGS LIGs of Veilleux et al. (1995; dashed line). The equivalent widths of the ULIGs are on average smaller than those of the lower-luminosity objects. Seyfert ULIGs may also have smaller equivalent widths than the other two classes of ULIGs, but the difference is not significant.

Fig. 12.— Distribution of the equivalent widths of Mg Ib $\lambda 5176$ as a function of the spectral types of the ULIGs in the present sample (solid line) and the BGS LIGs of Veilleux et al. (1995; dashed line). No significant differences between spectral types are detected among ULIGs. However, these equivalent widths are significantly smaller than those of non-active spiral galaxies (not shown here).

Fig. 13.— Distribution of the dereddened continuum colors, $(C6563/C4861)_0$, as a function of the spectral types of the ULIGs in the present sample (solid line) and the BGS LIGs of Veilleux et al. (1995; dashed line). The nuclear continuum of Seyfert ULIGs appears bluer on average than those of H II and LINER ULIGs, but these differences are not significant.

Fig. 14.— Dereddened continuum colors as a function of the dereddened H α luminosities. The meaning of the symbols is the same as in Fig. 5. A strong anti-correlation is observed.

Fig. 15.— Dereddened continuum colors as a function of the infrared luminosities. The meaning of the symbols is the same as in Fig. 5.

Fig. 16.— Distribution of the equivalent widths of H α in emission as a function of the spectral types of the ULIGs in the present sample (solid line) and the BGS LIGs of Veilleux et al. (1995; dashed line). The average equivalent width of the LINERs is marginally smaller than that of the H II galaxies, both at high and low infrared luminosities.

Fig. 17.— Distribution of the reddening-corrected H α luminosities as a function of the spectral types of the ULIGs in the present sample (solid line) and the BGS LIGs of Veilleux et al. (1995; dashed line). The LINERs are somewhat underluminous relative to Seyfert 2 galaxies, both at high and low infrared luminosities.

Fig. 18.— H α luminosities as a function of infrared luminosities. The meaning of the symbols is the same as in Fig. 5. Significant correlations are observed for all three spectral types.

Fig. 19.— Equivalent widths of H α as a function of infrared luminosities. The meaning of the symbols is the same as in Fig. 5. Significant correlations are observed among H II galaxies and LINERs.

Fig. 20.— Dereddened line ratios as a function of the size of the apertures. In all three panels, the asterisks (*) mark the nuclear values. The size of the extraction aperture increases along each segment (see introduction of §5).

Fig. 21.— Dereddened line ratios as a function of the distance from the nucleus. In all three panels, the asterisks (*) mark the nuclear values. The mid-distance of the extraction aperture increases along each segment (see introduction of §5).

Fig. 22.— Radial profiles of the mean values of (a) the color excesses, (b) the [O III] $\lambda 5007$ line widths, (c) the equivalent widths of $H\beta$ in absorption, (d) the equivalent widths of Mg Ib, (e) the dereddened continuum colors, (f) the $H\alpha$ luminosities, and (g) the equivalent widths of the $H\alpha$ emission. Stars, open circles, and filled circles represent data points from the HII, LINERs and Seyfert 2 ULIGs, respectively. The error bars in these figures indicate the standard deviation from the means in each radial bin.

TABLE 1
JOURNAL OF OBSERVATIONS

Obs. Date	Grating (l/mm)	Spectral Range (Å)	Resolution (Å)	Seeing (")	CCD
1992 Jul 5	600	4730 – 7740	8.3	1.1–1.3	Tek 1024 ²
1993 Mar 30-31	600	5670 – 8770	8.3	1.2–2.0	Tek 2048 ²
1993 May 14-15	600	4920 – 8270	8.3	1.2–1.8	Tek 2048 ²

TABLE 2
SPECTROSCOPIC 1 JY SURVEY

IRAS FSC (1)	z (2)	$\log\left(\frac{L_{\text{IR}}}{L_{\odot}}\right)$ (3)	Type (4)
New Data for 1 Jy Sample (39 objects) ^a			
07599+6508	0.149 (1)	12.46	Q,S1 (1,5,6)
08201+2801*	0.168 (1)	12.23	H (1)
08572+3915*	0.058 (1)	12.11	L (1,5)
10091+4704	0.246 (1)	12.67	L (1)
10494+4424*	0.092 (1)	12.13	L (1)
11029+3130	0.199 (1)	12.32	L (1)
11119+3257	0.189 (1)	12.58	S1 (1)
11223-1244*	0.199 (1)	12.59	S2 (1)
11506+1331*	0.127 (1)	12.28	H (1)
11582+3020*	0.223 (1)	12.56	L (1)
12072-0444*	0.129 (1)	12.35	S2 (1,5)
12112+0305*	0.073 (1)	12.28	L (1)
12540+5708	0.042 (1)	12.50	Q,S1 (1,5,6)
13218+0552	0.205 (1)	12.63	S1 (1,4)
13342+3932	0.179 (1)	12.37	S1 (1)
13428+5608*	0.037 (1)	12.10	S2 (1,5) ^b
13451+1232*	0.122 (1)	12.28	S2 (1)
13454-2956	0.129 (1)	12.21	S2 (1)
14060+2919*	0.117 (1)	12.03	H (1)
14070+0525	0.265 (1)	12.76	S2 (1)
14202+2615*	0.159 (1)	12.39	H (1)
14348-1447*	0.083 (1)	12.28	L (1,5)
14394+5332*	0.105 (1)	12.04	S2 (1)
15001+1433*	0.162 (1)	12.38	S2 (1)
15130-1958*	0.109 (1)	12.09	S2 (1)
15206+3342*	0.125 (1)	12.18	H (1)
15327+2340*	0.018 (1)	12.17	L (1,5) ^c
15462-0450	0.100 (1)	12.16	S1 (1)
16090-0139*	0.134 (1)	12.49	L (1)
16300+1558	0.242 (1)	12.63	L (1)
16333+4630*	0.191 (1)	12.35	L (1)
16468+5200*	0.150 (1)	12.02	L (1)
16474+3430*	0.111 (1)	12.11	H (1)
16487+5447*	0.104 (1)	12.12	L (1)
17028+5817*	0.106 (1)	12.10	L (1)
17044+6720*	0.135 (1)	12.13	L (1)
17068+4027*	0.179 (1)	12.30	H (1)
20414-1651*	0.086 (1)	12.14	H (1)
21329-2346*	0.125 (1)	12.09	L (1)
New Data for Extended 1 Jy Sample (6 objects)			
14378-3651*	0.068 (1)	12.07	L (1)
17208-0014*	0.043 (1)	12.35	H (1)
17574+0629*	0.109 (1)	12.11	H (1)
18470+3233*	0.079 (1)	12.02	H (1)
19297-0406*	0.084 (1)	12.31	H (1)
20087-0308*	0.105 (1)	12.36	L (1)

TABLE 2—*Continued*

IRAS FSC (1)	z (2)	$\log\left(\frac{L_{\text{IR}}}{L_{\odot}}\right)$ (3)	Type (4)
Previously Published Data for 1 Jy Sample			
01572+0009	0.163 (4)	12.53	Q,S1 (6)
05189–2524 [†]	0.042 (5)	12.07	S2 (5)
08559+1053	0.149 (3)	12.16	S2 (3)
12265+0219	0.159 (6)	12.73	Q,S1 (6)
13305–1739	0.148 (2)	12.21	S2 (2)
21219–1757	0.113 (3)	12.06	S1 (3)
22491–1808 [†]	0.076 (5)	12.09	H (5)

Column (1) – Target name. FSC is the prefix given to the name of all sources in the *IRAS* Faint Source Catalog (c.f. Moshir et al. 1992). Galaxies used for spatial information (§5) are flagged with asterisk (*) and galaxies used only for spectral classification (§4.1) are flagged with dagger (†).

Column (2) – Optical redshift. Numbers in parentheses are references.

Column (3) – Infrared luminosity (see text).

Column (4) – Spectral type: H II = HII galaxy, L = LINER, S2 = Seyfert 2, S1 = Seyfert 1, Q = quasar. Numbers in parentheses are references.

^aData for the 1 Jy and Extended 1 Jy objects are merged into a single list in subsequent tables.

^bThis object was classified as a LINER by Veilleux et al. (1995). The reclassification of this object is due to a slight change in the [O III] λ 5007/H β ratio which may be attributable to differences in the extraction apertures between the two sets of data. See Section 4.1.

^cThis object was classified as a Seyfert 2 by Veilleux et al. (1995). The present classification is considered more reliable because the data are of better quality and are less affected by centering errors. See Section 4.1.

REFERENCES.—For redshifts: (1) This work (see Paper I for a comparison of our redshifts with previous values from the literature), (2) Allen et al. 1991, (3) Hill et al. 1988, (4) MacKenty & Stockton 1984, (5) Sanders et al. 1988, (6) Schmidt 1963

REFERENCES.—For spectral type: (1) This work, (2) Allen et al. 1991, (3) Hill et al. 1988, (4) Low et al. 1988, (5) Veilleux et al. 1995, (6) Véron-Cetty & Véron 1989

TABLE 3
EMISSION-LINE FLUXES, LUMINOSITIES, AND ELECTRON DENSITIES

Name IRAS FSC (1)	$F_{H\alpha}$ (2)	$EW_{H\alpha}$ (3)	$L_{H\alpha}$ log (4)	$H\beta$ 4861 (5)	[O III] 5007 (6)	[O I] 6300 (7)	[N II] 6583 (8)	[S II] 6716 (9)	[S II] 6731 (10)	n_e cm ⁻³ (11)
07598+6508	37::	162::
08201+2801	0.36	83	8.30	0.21	0.14	0.05	0.47	0.19	0.10	...
08572+3915:NW	0.89	72	9.13	0.05	0.13	0.05	0.43	0.26	0.23	350
08572+3915:SE	0.40	41	8.70		0.05	0.13	0.02	0.38	0.15	...
10091+4704	0.18	29	9.19	0.08	0.09	0.09	0.80	0.70s
10494+4424	0.31	37	8.18	0.11	0.15	0.13	0.60	0.23	0.22	550
11029+3130	0.03	9	6.96	0.29	0.12	0.18	1.15	0.68s
11119+3257	117::	222::
11223-1244	0.20	40	10.33	0.02:	0.32	0.08	1.05	0.37	0.19	...
11506+1331	0.47	89	8.76	0.11	0.13	0.10	0.43	0.19	0.16	230
11582+3020	0.14	51	8.59	0.15	0.17	0.13	0.73	0.20	0.22	820
12072-0444	1.70	175	9.90	0.06	0.45	0.09	0.71	0.32	0.20	...
12112+0305	0.80	65	8.27	0.13	0.27	0.12	0.64	0.54s
12540+5708	135::	168::
13218+0552	1.98:	391	...	0.14:	0.29:	0.05:	0.25:	0.06:	0.04:	...
13342+3932	4.12	301	...	0.07	0.28	0.02	0.53	0.03	0.03	850
13428+5608	8.21	96	8.97	0.10	0.36	0.13	1.02	0.31	0.27	280
13451+1232	2.80	248	9.62	0.09	0.83	0.23	0.75	0.22	0.21	450
13454-2956	0.12	26	8.58	0.07	0.40	0.06	1.04	0.44s
14060+2919	3.03	194	9.25	0.14	0.11	0.04	0.46	0.17	0.16	370
14070+0525	0.11	26	9.76	0.04	0.19	0.13	0.82	0.32	0.41	410
14202+2615	1.20	170	9.03	0.16	0.13	0.04	0.46	0.17	0.13	170
14348-1447:SW	1.16	91	8.73	0.11	0.15	0.11	0.65	0.26	0.20	140
14348-1447:NE	0.49	46	8.40	0.10:	0.15	0.15	0.67	0.34	0.24	30
14378-3651	0.59	39	8.41	0.09	0.17	0.12	0.85	0.37s
14394+5332	4.49	159	9.36	0.13	0.43	0.20	0.94	0.43	0.19	...
15001+1433	0.64	70	8.89	0.13	0.48	0.06	0.65	0.22	0.23	640
15130-1958	1.05:	98	10.05	0.04:	0.88:	0.08:	0.84:	0.28:s
15206+3342	7.67	397	9.58	0.17	0.52	0.03	0.22	0.08	0.06	210
15327+2340	1.09	16	7.29	0.11:	0.13	0.18	2.39	1.06s
15462-0450	5.6:	168	...	0.18:	0.18:	0.01:	0.38:	0.07:s
16090-0139	1.31	128	9.66	0.07	0.08	0.08	0.77	0.24	0.16	...
16300+1558	0.22	40	8.89	0.12	0.15	0.11	0.60	0.32	0.19	...
16333+4630	0.49	100	8.98	0.12	0.20	0.06	0.58	0.24	0.17	10
16468+5200:W	0.15	47	8.28	0.12	0.08	0.02	0.65	0.32	0.35	820
16468+5200:E	0.09	30	8.40	0.09	0.10	0.06:	0.69	0.43	0.38	370
16474+3430	1.28	87	8.33	0.24	0.26	0.06	0.48	0.16	0.15	510
16487+5447	2.92	185	8.71	0.20	0.32	0.07	0.58	0.21	0.15	50
17028+5817:W	0.44	72	8.90	0.07	0.11	0.11	0.57	0.20	0.22	740
17028+5817:E	0.79	135	8.39	0.18	0.20	0.02	0.28	0.18	0.13	40

TABLE 3—*Continued*

Name IRAS FSC (1)	$F_{\text{H}\alpha}$ (2)	$EW_{\text{H}\alpha}$ (3)	$L_{\text{H}\alpha}$ log (4)	$\text{H}\beta$ 4861 (5)	[O III] 5007 (6)	[O I] 6300 (7)	[N II] 6583 (8)	[S II] 6716 (9)	[S II] 6731 (10)	n_e cm^{-3} (11)
17044+6720	0.57	99	8.63	0.14	0.37	0.10	0.62	0.23	0.13	...
17068+4027	0.91	227	9.71	0.08	0.17	0.03	0.34	0.22	0.15	...
17208-0014	1.79	51	8.96	0.06	0.05	0.05	0.46	0.19	0.14	100
17574+0629	2.16	278	9.30	0.11	0.21	0.04	0.34	0.13	0.07	...
18470+3233	2.23	162	8.99	0.11	0.13	0.05	0.44	0.17	0.11	...
19297-0406	0.64	92	8.86	0.08	0.05	0.08	0.56	0.20	0.16	240
20087-0308	0.45	37	8.85	0.05	0.10	0.18	1.02	0.52s
20414-1651	0.37	48	8.37	0.11	0.08	0.11	0.54	0.18	0.14	180
21329-2346	0.50	79	8.30	0.17	0.17	0.10	0.61	0.45s

Column (1) – Target name.

Column (2) – Absolute flux of $\text{H}\alpha$ in units of $10^{-14} \text{ erg s}^{-1} \text{ cm}^{-2}$.

Column (3) – Equivalent widths of the $\text{H}\alpha$ emission line in \AA derived in the rest frames of the objects.

Column (4) – Logarithms of the dereddened $\text{H}\alpha$ luminosities in units of the bolometric solar luminosity ($3.83 \times 10^{33} \text{ erg s}^{-1}$).

Column (5) – Flux of $\text{H}\beta$ relative to $\text{H}\alpha$. This is the weighted average of the values obtained from the standard plotting package of IRAF ('splot') and the fitting procedures, with weights estimated from the relative uncertainties in the two types of measurements (see §3).

Column (6) – Flux of [O III] $\lambda 5007$ relative to $\text{H}\alpha$.

Column (7) – Flux of [O I] $\lambda 6300$ relative to $\text{H}\alpha$.

Column (8) – Flux of [N II] $\lambda 6583$ relative to $\text{H}\alpha$.

Column (9) – Flux of [S II] $\lambda 6716$ relative to $\text{H}\alpha$. Entry followed by the letter “s” represents the sum of [S II] $\lambda 6716$ and [S II] $\lambda 6731$ relative to $\text{H}\alpha$.

Column (10) – Flux of [S II] $\lambda 6731$ relative to $\text{H}\alpha$.

Column (11) – Electron densities determined from the values of [S II] $\lambda 6716$ /[S II] $\lambda 6731$ and the five-level-atom calculations of De Robertis, Dufour, & Hunt (1987).

NOTE.— The emission line fluxes listed in Table 3 are normalized to the observed flux of narrow $\text{H}\alpha$. In Seyfert 1s (see Table 5), the $\text{H}\alpha$ flux, equivalent width, and luminosity refer to the sum of the narrow and broad components of $\text{H}\alpha$. The uncertainty on these measurements is typically of 5 – 10%, and colons (:) indicate values with relative uncertainties of 20 – 30%. Double colons (::) indicate values with relative uncertainties larger than 30% and these objects were not considered in the analysis because of the large uncertainties in the data.

TABLE 4
 ABSORPTION PROPERTIES, LINE WIDTHS, AND CONTINUUM LEVELS

Name IRAS FSC (1)	$EW(\text{\AA})$			$FWHM$ [O III] (5)	C4861 (6)	$r(C)$	
	H β (2)	Mg Ib (3)	Na ID (4)			(7)	(8)
07598+6508	32.2	22.6	...
08201+2801	...	1.3	4.6	510	0.50	0.44	0.52
08572+3915:NW	...	0.7	3.4	70	1.07	1.23	0.17
08572+3915:SE	...	0.2	2.7	...	0.77	0.99	0.20
10091+4704	0.8	2.2	3.2	360	0.57	0.62	0.28
10494+4424	8.2	0.1	4.1	...	0.52	0.83	0.56
11029+3130	5.6:	1.5	2.7	...	0.35	0.34	0.89
11119+3257	2.03	4.74	...
11223-1244	2.8	2.3	6.9	960	0.36	0.50	0.10
11506+1331	1.1	0.8	4.9	80	0.44	0.53	0.39
11582+3020	0.5:	0.2	4.0	350	0.33	0.27	0.38
12072-0444	0.5:	0.3	2.1	500	0.81	0.97	0.22
12112+0305	1.2:	1.5	4.0	...	1.26	1.23	0.39
12540+5708	85.0	75.1	...
13218+0552	...	2.4	0.8	1430	0.59	0.51	...
13342+3932	0.5:	0.8	2.4	420	1.87	1.37	...
13428+5608	0.3	0.7	4.9	480	7.76	8.55	0.33
13451+1232	0.2	1.5	0.5	1250	0.80	1.13	0.40
13454-2956	...	0.2	1.9	70	0.47	0.46	0.21
14060+2919	0.7	1.2	2.8	200	1.56	1.56	0.41
14070+0525	0.7	1.5	4.6	...	0.34	0.42	0.15
14202+2615	0.3	1.4	3.5	160	0.77	0.71	0.42
14348-1447:SW	3.4	0.6	4.8	440	1.00	1.28	0.42
14348-1447:NE	3.7	0.4	3.9	100	0.95	1.08	0.36
14378-3615	0.2	3.3	7.8	...	1.20	1.52	0.36
14394+5332	0.4	0.2	3.9	1870	2.41	2.83	0.46
15001+1433	0.6	1.2	4.2	280	0.96	0.91	0.38
15130-1958	0.2:	0.2	3.6	1100	0.92	1.07	0.13
15206+3342	0.1	0.2	1.9	60	2.41	1.93	0.38
15327+2340	2.6:	2.7	5.8	...	4.50	6.93	0.54
15462-0450	...	0.3	0.2:	1560	3.24	3.33	...
16090-0139	0.5	1.8	4.4	150	0.79	1.02	0.28
16300+1558	2.1	1.0	5.5	120	0.56	0.54	0.35
16333+4630	0.7	0.4	3.4	450	0.45	0.49	0.42
16468+5200:W	4.3	...	0.33	0.32	0.37
16468+5200:E	0.28	0.31	0.30
16474+3430	2.2	0.4	1.6	...	1.92	1.47	0.52
16487+5447	0.1	1.4	1.2	340	2.16	1.58	0.45
17028+5817:W	0.9	1.5	5.9	80	0.46	0.62	0.31
17028+5817:E	0.9	2.2	2.5	120	0.61	0.59	0.48

TABLE 4—*Continued*

Name IRAS FSC (1)	$EW(\text{\AA})$			$FWHM$ [O III] (5)	C4861 (6)	$r(C)$	
	H β (2)	Mg Ib (3)	Na ID (4)			(7)	(8)
17044+6720	0.5	0.9	0.8	280	0.61	0.58	0.40
17068+4027	0.9	1.7	3.9	440	0.35	0.40	0.26
17208–0014	2.1	1.1	8.4	60	1.77	3.49	0.34
17574+0629	0.8	1.5	0.7	240	0.70	0.78	0.35
18470+3233	0.1	0.3	2.9	230	1.27	1.38	0.35
19297–0406	0.8	1.2	4.5	190	0.42	0.70	0.38
20087–0308	2.2:	4.7	9.8	160	0.73	1.19	0.39
20414–1651	1.1	0.5	3.6	...	0.57	0.77	0.40
21329–2346	3.1	2.2	2.9	290	0.87	0.63	0.37

Column (1) – Target name.

Column (2) – Equivalent widths of the H β absorption feature in \AA derived from the fitting method and in the rest frames of the objects. The typical uncertainties on these measurements are about 10 – 20%, and for some of the objects with strong H β emission line they are \sim 30% (values flagged with a colon).

Column (3) – Equivalent widths of the Mg Ib λ 5176 absorption feature in \AA derived in the rest frames of the objects. The typical uncertainties on these measurements are about 10 – 20%, and for some of the objects they are \sim 30% (values flagged with a colon).

Column (4) – Equivalent widths of the H β absorption feature in \AA derived in the rest frames of the objects. The typical uncertainties on these measurements are about 10 – 20%, and for some of the objects they are \sim 30% (values flagged with a colon).

Column (5) – Line widths of [O III] λ 5007 in km s^{-1} after correction for the finite instrument resolution of the data using the quadrature method (see §4.4).

Column (6) – Observed continuum levels near 4861 \AA in units of $10^{-16} \text{ erg s}^{-1} \text{ cm}^{-2} \text{\AA}^{-1}$.

Column (7) – Observed continuum levels near 6563 \AA in units of $10^{-16} \text{ erg s}^{-1} \text{ cm}^{-2} \text{\AA}^{-1}$.

Column (8) – Dereddened continuum ratios ($[C6563/C4861]_0$).

TABLE 5
OBSERVED AND DEREDDENED LINE RATIOS AND SPECTRAL CLASSIFICATION

Name IRAS FSC (1)	$\frac{H\alpha}{H\beta}$ log (2)	$E(B - V)$ (3)	$\frac{[OIII]}{H\beta}$ log (4)	$\frac{[NII]}{H\alpha}$ log (5)	$\frac{[SII]}{H\alpha}$ log (6)	$\frac{[OI]}{H\alpha}$ log (7)	Spectral Type			
							[N II] (8)	[S II] (9)	[O I] (10)	Adopt (11)
07598+6508				S1
				
08201+2801	0.68	0.53	-0.19	-0.32	-0.54	-1.32	H	H	H	H
	0.45		-0.21	-0.33	-0.55	-1.29				
08572+3915:NW	1.33	1.94	0.46	-0.37	-0.31	-1.30	H	L	L	L:
	0.49		0.36	-0.38	-0.37	-1.20				
08572+3915:SE	1.29	1.85	0.42	0.00	-0.28	-1.78	L	L	H	L:
	0.49		0.33	-0.01	-0.34	-1.69				
10091+4704	1.08	1.36	0.05	-0.10	-0.16	-1.06	L	H	L	L:
	0.49		-0.02	-0.10	-0.20	-0.99				
10494+4424	0.94	1.04	0.12	-0.22	-0.35	-0.90	L	L	L	L
	0.49		0.07	-0.23	-0.38	-0.85				
11029+3130	0.53	0.10	-0.37	0.06	-0.17	-0.74	L	L	L	L
	0.49		-0.38	0.06	-0.17	-0.74				
11119+3257	-0.04				S1
	0.49					
11223-1244	1.65	2.68	1.16	0.02	-0.25	-1.10	S2	S2	S2	S2
	0.49		1.03	0.01	-0.34	-0.96				
11506+1331	0.98	1.13	0.08	-0.37	-0.46	-0.98	H	H	L	H:
	0.45		0.02	-0.38	-0.50	-0.92				
11582+3020	0.82	0.76	0.04	-0.13	-0.38	-0.89	L	L	L	L
	0.49		0.00	-0.14	-0.40	-0.85				
12072-0444	1.23	1.71	0.88	-0.15	-0.29	-1.07	S2	S2	S2	S2
	0.49		0.80	-0.15	-0.34	-0.98				
12112+0305	0.89	0.92	0.32	-0.19	-0.27	-0.93	L	L	L	L
	0.49		0.28	-0.20	-0.29	-0.89				
12540+5708				S1
	0.49					
13218+0552	0.85	0.83	0.31	-0.61	-0.99	-1.35				S1
	0.49		0.27	-0.61	-1.01	-1.30				
13342+3932	1.17	1.57	0.62	-0.28	-1.22	-1.77				S1
	0.49		0.55	-0.29	-1.27	-1.69				
13428+5608	1.02	1.22	0.57	0.01	-0.24	-0.88	S2	S2	S2	S2
	0.49		0.51	0.00	-0.27	-0.82				
13451+1232	1.04	1.26	0.96	-0.12	-0.37	-0.65	S2	S2	S2	S2
	0.49		0.90	-0.13	-0.41	-0.58				
13454-2956	1.16	1.54	0.76	0.02	-0.36	-1.23	S2	S2	S2	S2
	0.49		0.68	0.01	-0.41	-1.15				
14060+2919	0.84	0.90	-0.12	-0.34	-0.49	-1.42	H	H	H	H
	0.45		-0.17	-0.34	-0.51	-1.38				
14070+0525	1.39	2.08	0.67	-0.09	-0.14	-0.90	S2	S2	S2	S2
	0.49		0.57	-0.10	-0.20	-0.79				
14202+2615	0.80	0.79	-0.10	-0.34	-0.53	-1.39	H	H	H	H
	0.45		-0.14	-0.34	-0.55	-1.35				
14348-1447:SW	0.99	1.15	0.17	-0.18	-0.23	-0.83	L	L	L	L
	0.49		0.11	-0.18	-0.27	-0.77				

TABLE 5—*Continued*

Name IRAS FSC (1)	$\frac{H\alpha}{H\beta}$ log (2)	$E(B - V)$ (3)	$\frac{[OIII]}{H\beta}$ log (4)	$\frac{[NII]}{H\alpha}$ log (5)	$\frac{[SII]}{H\alpha}$ log (6)	$\frac{[OI]}{H\alpha}$ log (7)	Spectral Type			
							[N II] (8)	[S II] (9)	[O I] (10)	Adopt (11)
14348–1447:NE	0.97	1.11	0.15	–0.18	–0.34	–0.98	L	L	L	L
	0.49		0.09	–0.19	–0.38	–0.92				
14378–3651	1.04	1.26	0.28	–0.07	–0.44	–0.94	L	H	L	L:
	0.49		0.21	–0.07	–0.48	–0.87				
14394+5332	0.89	0.93	0.53	–0.03	–0.21	–0.71	S2	S2	S2	S2
	0.49		0.49	–0.03	–0.24	–0.66				
15001+1433	0.89	0.91	0.57	–0.19	–0.35	–1.21	S2	S2	S2	S2
	0.49		0.53	–0.19	–0.37	–1.16				
15130–1958	1.45	2.23	1.40	–0.08	–0.55	–1.13	S2	S2	S2	S2
	0.49		1.29	–0.09	–0.62	–1.01				
15206+3342	0.78	0.75	0.49	–0.65	–0.86	–1.60	H	H	H	H
	0.45		0.45	–0.65	–0.88	–1.56				
15327+2340	0.95	1.05	0.06	0.38	0.02	–0.74	L	L	L	L
	0.49		0.01	0.38	–0.01	–0.68				
15462–0450	0.75	0.60	0.00	–0.42	–1.15	–1.84				S1
	0.49		–0.02	–0.42	–1.17	–1.81				
16090–0139	1.16	1.55	0.08	–0.11	–0.39	–1.11	L	H	L	L:
	0.49		0.01	–0.12	–0.44	–1.03				
16300+1558	0.92	1.00	0.09	–0.22	–0.29	–0.97	L	L	L	L
	0.49		0.04	–0.23	–0.32	–0.92				
16333+4630	0.91	0.96	0.20	–0.24	–0.38	–1.19	L	L	L	L
	0.49		0.16	–0.24	–0.41	–1.15				
16468+5200:W	0.92	0.99	–0.19	–0.19	–0.18	–1.69	L	L	H	L:
	0.49		–0.24	–0.20	–0.21	–1.64				
16468+5200:E	1.07	1.33	0.06	–0.16	–0.09	–1.24	L	L	L	L
	0.49		–0.01	–0.17	–0.13	–1.18				
16474+3430	0.62	0.39	0.04	–0.32	–0.51	–1.25	H	H	L	H:
	0.45		0.03	–0.32	–0.52	–1.23				
16487+5447	0.70	0.48	0.20	–0.24	–0.44	–1.16	L	H	L	L:
	0.49		0.18	–0.24	–0.46	–1.14				
17028+5817:W	1.13	1.47	0.16	–0.25	–0.38	–0.97	L	H	L	L:
	0.49		0.09	–0.25	–0.42	–0.90				
17028+5817:E	0.76	0.70	0.05	–0.56	–0.51	–1.64	H	H	H	H
	0.45		0.01	–0.56	–0.53	–1.61				
17044+6720	0.87	0.86	0.43	–0.21	–0.44	–0.99	L	L	L	L
	0.49		0.39	–0.21	–0.46	–0.95				
17068+4027	1.10	1.48	0.33	–0.46	–0.44	–1.47	H	H	H	H
	0.45		0.26	–0.47	–0.48	–1.40				
17207–0014	1.21	1.75	–0.08	–0.34	–0.48	–1.31	H	H	H	H
	0.45		–0.16	–0.35	–0.54	–1.22				
17574+0629	0.95	1.15	0.27	–0.48	–0.69	–1.44	H	H	H	H
	0.45		0.21	–0.48	–0.73	–1.38				
18470+3233	0.95	1.13	0.06	–0.36	–0.56	–1.34	H	H	H	H
	0.45		0.01	–0.37	–0.59	–1.29				
19297–0406	1.10	1.49	–0.16	–0.25	–0.44	–1.09	H	H	L	H:
	0.45		–0.23	–0.26	–0.49	–1.01				

TABLE 5—*Continued*

Name IRAS FSC (1)	$\frac{H\alpha}{H\beta}$ log (2)	$E(B - V)$ (3)	$\frac{[OIII]}{H\beta}$ log (4)	$\frac{[NII]}{H\alpha}$ log (5)	$\frac{[SII]}{H\alpha}$ log (6)	$\frac{[OI]}{H\alpha}$ log (7)	Spectral Type			
							[N II] (8)	[S II] (9)	[O I] (10)	Adopt (11)
20087–0308	1.11 0.49	1.43	0.26 0.17	0.01 0.00	–0.28 –0.34	–0.75 –0.65	L	L	L	L
20414–1651	0.98 0.45	1.21	–0.11 –0.17	–0.27 –0.27	–0.50 –0.54	–0.97 –0.90	H	H	L	H:
21329–2346	0.78 0.49	0.67	0.00 –0.03	–0.21 –0.22	–0.35 –0.37	–0.98 –0.95	L	L	L	L

Column (1) – Target name.

Column (2) – Logarithm of $H\alpha/H\beta$.

Column (3) – Color excesses determined from the emission-line Balmer decrements (cf. §4.2).

Column (4) – Logarithm of reddening-corrected $[O III] \lambda 5007/H\beta$.

Column (5) – Logarithm of reddening-corrected $[N II] \lambda 6583/H\alpha$.

Column (6) – Logarithm of reddening-corrected $[S II] \lambda\lambda 6716, 6731 /H\alpha$.

Column (7) – Logarithm of reddening-corrected $[O I] \lambda 6300/H\alpha$.

Columns (8) through (11) – Optical spectral types determined from the diagrams of Veilleux & Osterbrock (1987) involving $[N II] \lambda 6583$ [column (8)], $[S II] \lambda\lambda 6716, 6731$ [column (9)], and $[O I] \lambda 6300$ [column (10)]. Column (11) lists the adopted spectral type. Meaning of the symbols: H = H II galaxies, L = LINER (‘low-ionization nuclear emission-line regions’), S2 = Seyfert 2 galaxies, and S1 = Seyfert 1 galaxies. A colon (:) indicates galaxies with line ratios that do not correspond to the same spectral type in all three diagrams of Veilleux & Osterbrock (1987). See §4.1 for further detail.

NOTE.—The emission line ratios listed in Table 3 are normalized to the observed flux of narrow $H\alpha$ or $H\beta$. In Seyfert 1s, the ratios are normalized to the sum of the narrow and broad components of $H\alpha$ or $H\beta$. These ratios are only listed for illustrative purposes since they cannot be used for spectral classification. The uncertainty on the emission line ratios is typically $\pm 10\%$. For entries with a colon (:) the uncertainty is approximately $\pm 25\%$.

TABLE 6
SPECTRAL CLASSIFICATION AS A FUNCTION OF L_{ir}

$\log \left(\frac{L_{\text{ir}}}{L_{\odot}} \right)$	<11 ^a	11–11.99 ^a	12–12.29	12.3–12.9
Number	29	68	27	20
H II region (%)	62	53	33	20
AGN-like (%)	38	47	67	80
Seyfert 1 (%)	0	2	4	25
Seyfert 2 (%)	7	13	22	20
LINER (%)	31	32	41	35

^aData from luminous infrared galaxies in the BGS studied by VKSMS.

TABLE 7
RADIAL PROFILES OF THE SPECTRAL PARAMETERS

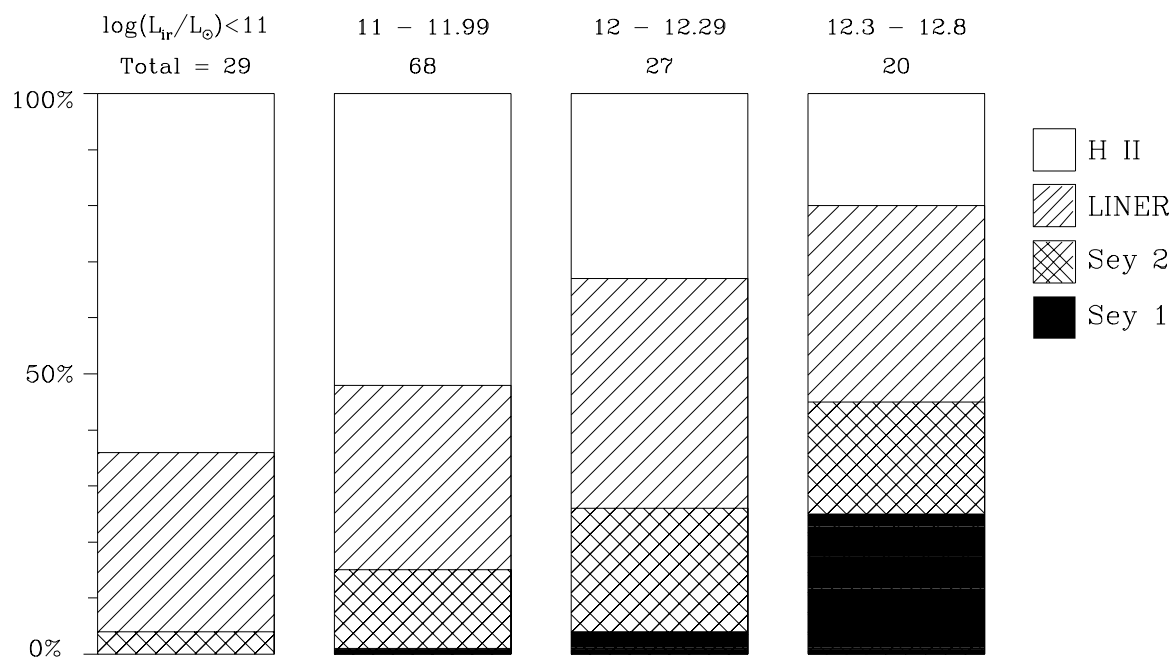
Type ^a	0 – 1 kpc			1 – 2 kpc			2 – 4 kpc			4 – 8 kpc		
	Mean	Median	No. ^b	Mean	Median	No.	Mean	Median	No.	Mean	Median	No.
<i>E(B – V)</i>												
H II	1.16±0.42	1.15	6	1.30±0.56	1.27	6	0.91±0.35	0.82	11	0.80±0.48	0.97	5
LINER	1.29±0.52	1.43	9	1.41±0.67	1.27	8	1.15±0.52	1.13	12	0.74±0.57	0.63	4
Sey 2	1.64±0.92	1.25	3	1.30±0.48	1.10	3	1.09±0.96	0.92	6	0.98±0.98	0.98	1
<i>FWHM</i> ([O III])												
H II	130±110	190	6	160±160	160	6	320±230	310	11	470±440	460	5
LINER	100±130	40	9	260±240	190	8	230±220	190	13	310±290	280	4
Sey 2	1140±740	1130	3	1200±620	1040	3	900±630	650	6	200±290	200	2
<i>EW</i> (H β)												
H II	1.0±0.8	1.0	6	1.7±1.6	1.5	6	2.0±1.9	1.8	12	1.8±1.2	1.9	3
LINER	1.9±2.5	1.2	9	2.3±2.1	1.9	8	2.1±2.0	1.1	13	2.7±2.1	2.5	4
Sey 2	0.3±0.1	0.3	3	0.4±0.3	0.2	3	0.8±0.7	0.7	6	2.5±2.6	2.5	2
<i>EW</i> (Mg Ib)												
H II	1.2±1.0	0.7	6	1.2±1.3	0.8	6	0.9±0.7	0.6	12	0.7±0.6	0.6	5
LINER	2.1±1.8	1.9	9	1.6±1.3	1.3	8	1.6±1.0	1.6	13	3.0±3.1	1.8	4
Sey 2	0.4±0.3	0.4	3	0.7±0.5	0.7	3	1.2±0.8	0.9	6	1.1±0.1	1.1	2
<i>(C6563/C4861)₀</i>												
H II	0.40±0.05	0.39	6	0.36±0.11	0.36	6	0.44±0.09	0.45	11	0.42±0.29	0.38	5
LINER	0.39±0.22	0.39	9	0.35±0.16	0.39	8	0.45±0.34	0.36	12	0.61±0.26	0.58	4
Sey 2	0.30±0.19	0.33	3	0.33±0.15	0.38	3	0.50±0.39	0.41	6	0.29±0.11	0.29	2
<i>log (L_{Hα}/L_{\odot})₀</i>												
H II	8.65±0.28	8.69	6	8.54±0.25	8.55	6	8.77±0.57	8.35	11	8.90±0.27	8.94	5
LINER	8.65±0.42	8.54	9	8.70±0.69	8.36	8	8.70±0.62	8.44	12	8.75±0.79	7.81	4
Sey 2	9.89±0.64	9.20	3	8.97±0.34	9.12	3	9.38±0.89	8.37	6	8.74±0.13	8.74	2
<i>EW</i> (H α)												
H II	125±81	99	6	109±79	89	6	127±115	77	12	140±101	110	5
LINER	78±53	65	9	68±46	58	8	62±37	50	13	63±19	63	4
Sey 2	129±37	112	3	98±59	72	3	61±21	71	6	37±33	37	2

^aNuclear spectral type.

^bNumber of objects used for statistics.

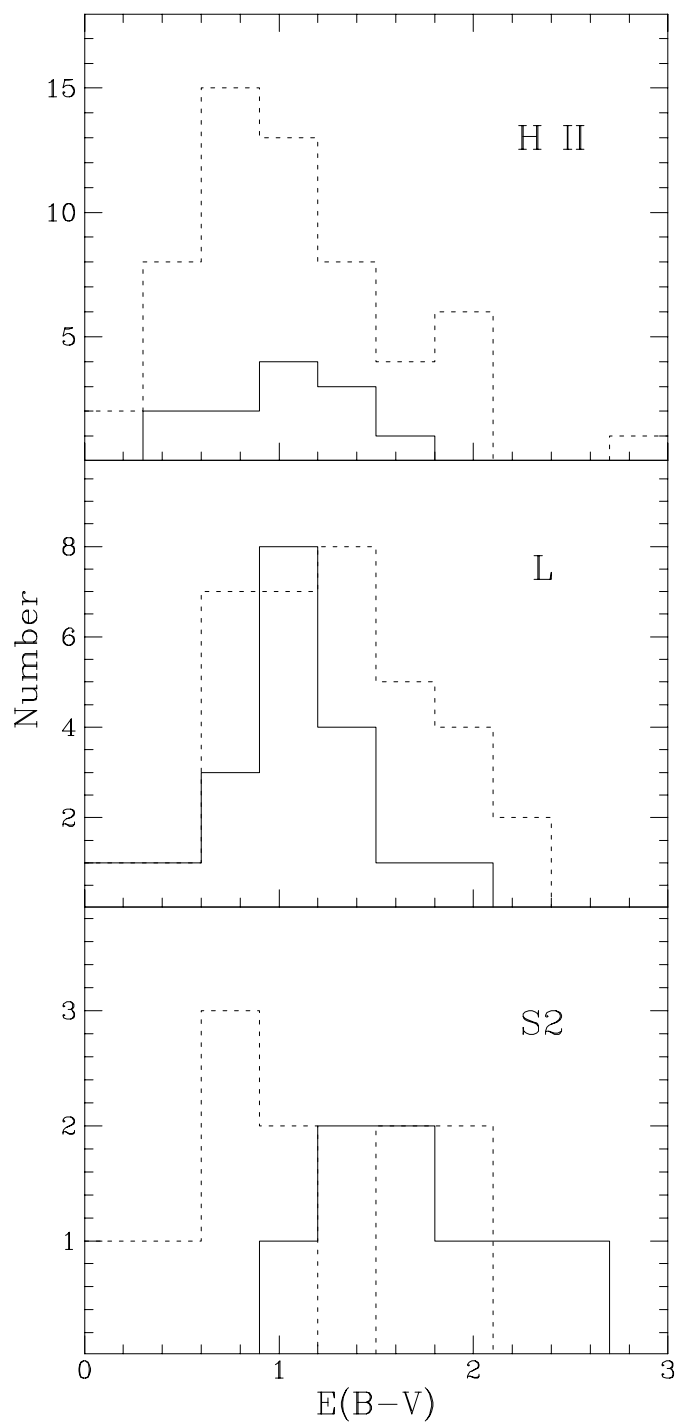
This figure "fig1_3.jpg" is available in "jpg" format from:

<http://arxiv.org/ps/astro-ph/9806149v1>



This figure "fig1_4.jpg" is available in "jpg" format from:

<http://arxiv.org/ps/astro-ph/9806149v1>



This figure "fig1_5.jpg" is available in "jpg" format from:

<http://arxiv.org/ps/astro-ph/9806149v1>

